



HAL
open science

Quantitative analysis of spin wave dynamics in ferrimagnets across compensation points

Eloi Haltz, Sachin Krishnia, Léo Berges, Raphaël Weil, Alexandra Mougin,
André Thiaville, Joao Sampaio

► **To cite this version:**

Eloi Haltz, Sachin Krishnia, Léo Berges, Raphaël Weil, Alexandra Mougin, et al.. Quantitative analysis of spin wave dynamics in ferrimagnets across compensation points. *Physical Review B*, 2022, 105 (10), pp.104414. 10.1103/PhysRevB.105.104414 . hal-03635125

HAL Id: hal-03635125








<https://hal.science/hal-03635125v1>

Submitted on 8 Apr 2022

HAL is a multi-disciplinary open access archive for the deposit and dissemination of scientific research documents, whether they are published or not. The documents may come from teaching and research institutions in France or abroad, or from public or private research centers.

L'archive ouverte pluridisciplinaire **HAL**, est destinée au dépôt et à la diffusion de documents scientifiques de niveau recherche, publiés ou non, émanant des établissements d'enseignement et de recherche français ou étrangers, des laboratoires publics ou privés.

Quantitative analysis of spin wave dynamics in ferrimagnets across compensation points

Eloi Haltz ^{1,2}, João Sampaio ^{1,*}, Sachin Krishna ¹, Léo Berges ¹, Raphaël Weil ¹,
Alexandra Mougin ¹ and André Thiaville ¹

¹Laboratoire de Physique des Solides, Université Paris-Saclay, CNRS, 91405 Orsay, France

²School of Physics and Astronomy, University of Leeds, Leeds LS2 9JT, England, United Kingdom



(Received 7 December 2021; revised 22 February 2022; accepted 24 February 2022; published 14 March 2022)

Rare-earth transition-metal ferrimagnets have two strongly coupled sublattices of distinct chemical nature, which give rise to complex and fast dynamics of great interest to spintronics. However, the dynamics of ferrimagnets remains less understood than ferromagnets. We measure the spin wave (SW) spectra of a GdFeCo film by Brillouin light scattering spectroscopy (BLS) across its compensation temperatures—temperatures at which either the sublattices' magnetizations or their angular moments cancel out, mimicking an antiferromagnet. We find two SW modes per wave vector with complex thermal dependencies, which cross at a field-dependent temperature. We develop an analytical model based on two sublattices corresponding to the rare earth and the transition metal, which reproduces quantitatively the SW spectra and their evolution with temperature and field. This validates the proposed energy and dynamical model of the ferrimagnet, and demonstrates the usefulness of BLS in the study of this promising class of materials.

DOI: [10.1103/PhysRevB.105.104414](https://doi.org/10.1103/PhysRevB.105.104414)

I. INTRODUCTION

The fast magnetization dynamics of antiferromagnets (AFs) and ferrimagnets, caused by the strong coupling of two or more magnetic sublattices, makes these materials very interesting for spintronic applications, including fast magnetic textures propagation or THz oscillators [1]. However, the modeling of their dynamics is far less developed than for ferromagnets. Moreover, AFs are hard to probe and excite. Unlike AFs, rare-earth transition-metal (RE-TM) ferrimagnets have large magneto-optical and spintronic effects, and the balance between their distinct sublattices can be tuned with temperature. This makes them ideal for applications and for the study of multilattice dynamics. Indeed, the sublattice moments in RE-TMs vary differently with temperature, causing both the net magnetization (M_S) and the net angular momentum (L_S) to also vary. Two remarkable temperatures appear: the magnetic and the angular compensation temperatures (T_{MC} and T_{AC}) where, respectively, M_S or L_S vanishes [2–5]. Previous studies have reported a large and complex variation of the spin wave (SW) frequencies with the balance between sublattices [6–10]. Different approaches have been used to model the ferrimagnetic dynamics of RE-TMs, its internal energy and dynamics: the effective ferromagnet model [11,12] (see also Appendix A), AF-inspired models that describe the system in terms of the Néel and magnetization vectors (\mathbf{l} , \mathbf{m}) [13], and models based on two distinct but coupled sublattices of RE and TM moments [7]. The SW spectrum, and its variation with field and temperature, provides a thorough test for these different models: it is sensitive to the different interactions (e.g., anisotropy and interlattice exchange coupling) and to the details of the dynamics that determine the properties of the different SW modes.

II. EXPERIMENTAL RESULTS

A GdFeCo (5 nm)/Al (5 nm) thin film with perpendicular magnetic anisotropy was coevaporated under ultrahigh vacuum on a Si/SiOx (100 nm) substrate [4]. The alloy composition [nominally Gd₄₀(Fe₈₅Co₁₅)₆₀] was optimized to have both T_{MC} and T_{AC} easily reachable. Figure 1(a) shows the variation with T of M_S (measured by superconducting quantum interference vibrating sample magnetometer) and of the perpendicular anisotropy field (H_K , measured via the anomalous Hall effect). The vanishing of M_S and the divergence of H_K at 311 K are a direct signature of the T_{MC} . By using the mean field model [2,4], it is possible to reproduce the measured $M_S(T)$ and estimate the magnetization of each sublattice, $M_{TM}(T)$ and $M_{RE}(T)$. The mean field model also predicts that $T_{AC} \approx 342$ K, consistent with previous measurements [5]. It has also been shown that such samples can exhibit a small internal Dzyaloshinskii-Moriya interaction (DMI) [14,15].

To study the SW properties, we measured the spectrum of inelastic light scattering by magnons [Brillouin light scattering (BLS)] (see Supplemental Material [16]). Through the Stokes (S) and the anti-Stokes (AS) processes, the incident photons can generate and absorb SW modes with a wave vector $\mathbf{k}_S = -\mathbf{k}_{AS}$. The frequency of the scattered light is shifted by the SW frequency, producing peaks at $f_{AS} > 0$ and $f_S < 0$ in the BLS spectrum. A magnetic field H along $\hat{\mathbf{y}}$ [Fig. 1(b)] is applied to counteract the perpendicular anisotropy and measure the SW in the Damon-Eshbach geometry ($\mathbf{k} \parallel \hat{\mathbf{x}}$ and $\mathbf{m} \parallel \hat{\mathbf{y}}$), which is convenient to measure the SW chirality [17,18].

The top panels of Fig. 1(c) show BLS spectra measured with $\mu_0 H = 0.56$ T at different temperatures, normalized to their maximum point. Considering first $T = 341$ K, four peaks are clearly visible at approximately ± 8.5 [“low frequency” (LF)] and ± 41 GHz [“high frequency” (HF)], two of which are S modes ($f < 0$) and two of which are AS modes

*joao.sampaio@universite-paris-saclay.fr

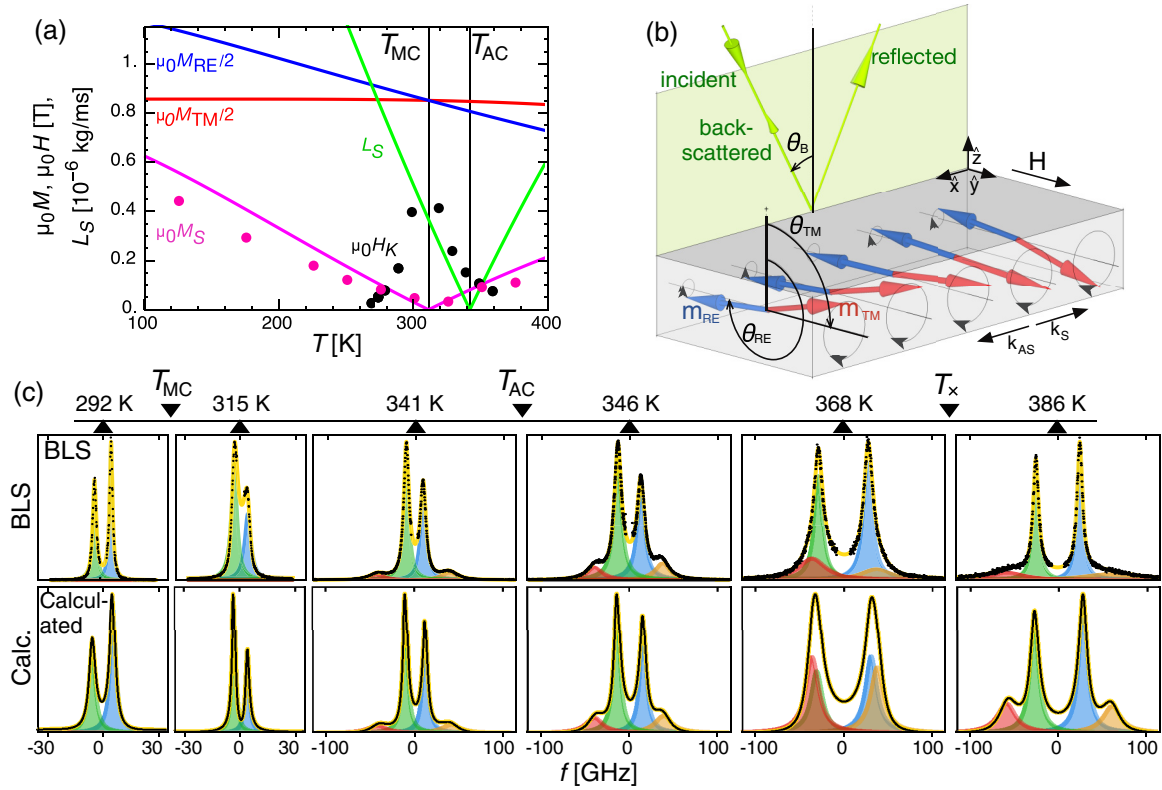


FIG. 1. (a) Measured magnetization M_S (pink dots) and anisotropy field H_K (black dots) vs temperature T . Lines are the results of the mean-field model: M_{TM} (red), M_{RE} (blue), $|M_S| = |M_{TM} - M_{RE}|$ (pink), and L_S (green). (b) Damon-Eshbach configuration used in the BLS measurements. (c) Experimental (top) and calculated (bottom) BLS spectra (black) with $\mu_0 H = 0.56$ T, at different temperatures and frequency ranges. The fitted peaks are shown individually by the filled curves (red, green, blue, and yellow) and summed together (yellow line).

($f > 0$). The presence of four modes (two per propagation direction) is a manifestation of two sublattices with a finite coupling. Some spectra at the lowest temperatures were taken with a narrower frequency range to increase instrumental resolution and better measure the LF peaks; in these, the HF peaks do not appear [16].

To extract the properties of these overlapping peaks, we fit the spectra with the sum of four asymmetric Lorentzian functions defined as $\mathcal{L}(f) = A \frac{1 + \epsilon(f - f_0)/\delta}{1 + (f - f_0)^2/\delta^2}$, where $\delta > 0$ (the width), f_0 (peak position), A (amplitude), and ϵ (asymmetry) are parameters of each peak. This sum is shown in yellow and the individual peaks are shown as filled curves in Fig. 1(c). Figure 2(a) shows the significant thermal evolution of f_0 (circles) and δ (vertical bars), extracted from the fits, for $\mu_0 H = 0.56$ T. We observe two S and two AS across the whole temperature range, except in the spectra taken with the restricted frequency range. Additionally, only two peaks are observed at a temperature that we name $T_x \approx 365$ K, where the frequencies of the two modes cross. Note that T_x seems distinct from $T_{AC} \approx 342$ K.

The frequency of the LF peaks is lowest around T_{MC} , showing two minima around 300 and 320 K on either side of T_{MC} , Fig. 2(b). This temperature interval coincides with the expected reorientation range, where $H < H_K(T)$ and thus where the magnetization is not perfectly in plane [Fig. 2(c)] and the geometry deviates from Damon-Eshbach. The minima of the resonant frequency occurring at the reorientation points correspond to the soft mode expected at $k = |\mathbf{k}| = 0$.

Figure 2(d) shows the difference in frequency between the S and AS modes ($\Delta f = |f_{AS}| - |f_S|$) for the LF and HF peaks. The data for the HF peaks are noisier due to their much lower amplitude and larger width. A nonzero Δf is a direct signature of an energy contribution that is odd in \mathbf{k} , due to DMI in this case [19]. The sign of Δf reflects the chirality of the SW modes. For LF, Δf changes sign twice with temperature, once progressively near T_{MC} and again, abruptly, at T_x . However, as we will see below, the change at T_{MC} does not correspond to a chirality reversal. Interestingly, the Δf of the HF peaks seems of opposite sign, which indicates that the two modes have opposite chirality [10]. Also, $|\Delta f|$ of the LF is approximately constant in temperature, except in the reorientation range or close to T_x .

III. MODELING FERRIMAGNETIC RESONANCE

A. Full model of BLS spectra

We model the ferrimagnetic system with two coupled Landau-Lifshitz-Gilbert (LLG) equations and two magnetization vector fields, corresponding to the RE and TM moments, following an approach used to analyze the ferromagnetic resonance (FMR) of compensated ferrimagnetic garnets and ferrites [6,7]. The system energy (U) is the sum of terms corresponding to the TM sublattice (exchange stiffness A_{TM} , DMI D_{TM} , uniaxial anisotropy K_{TM} , Zeeman energy), analogous terms for the RE sublattice, an exchange interlattice

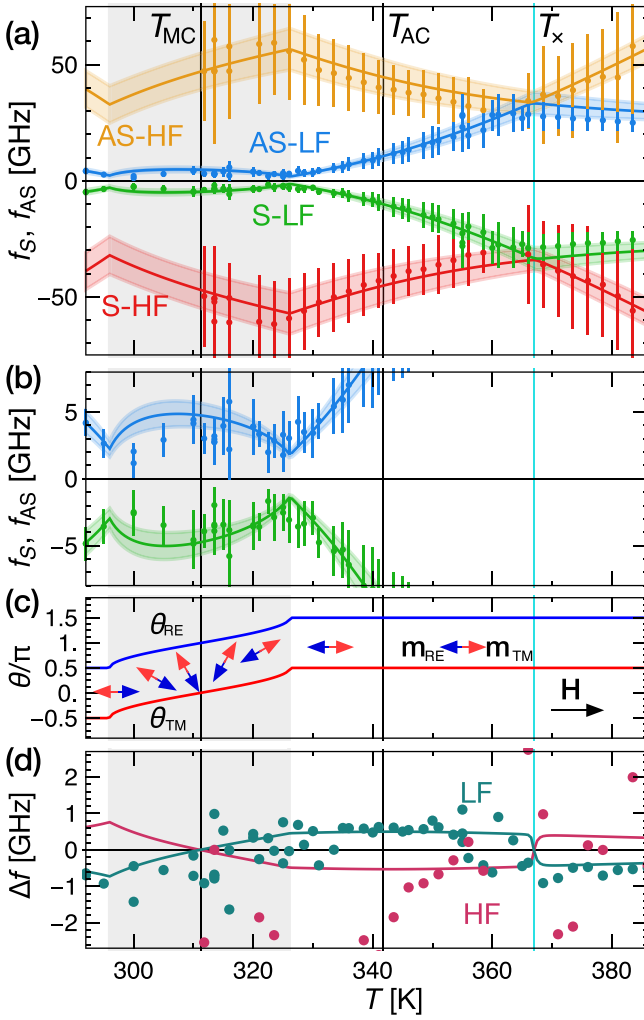


FIG. 2. (a) Peak centers f_0 (points) and widths δ (vertical bars) vs T , extracted from fits as those shown in Fig. 1(c). Lines and shaded envelopes are the frequency and peak width calculated with the Smit-Beljers method. (b) Same data as in panel (a) showing the LF peak in more detail. (c) Calculated equilibrium magnetization angles of the TM (θ_{TM}) and RE (θ_{RE}) sublattices vs T ($\mu_0 H = 0.56$ T). The reorientation range is shaded in all panels. (d) Frequency difference $\Delta f = |f_{\text{AS}}| - |f_{\text{S}}|$ for the LF and HF peaks vs T . The lines are the prediction of the Smit-Beljers method.

interaction (J), and dipolar interactions:

$$U = \sum_{i=\text{TM,RE}} [A_i \nabla^2 \mathbf{m}_i + D_i (m_{ix} \partial_x m_{iz} - m_{iz} \partial_x m_{ix}) - K_i m_{i,z}^2 - \mu_0 M_i \mathbf{H} \cdot \mathbf{m}_i] + J \mathbf{m}_{\text{TM}} \cdot \mathbf{m}_{\text{RE}} + U_{\text{demag}}. \quad (1)$$

We calculate the SW modes with two methods. First, we calculate the BLS spectral intensity, which is expected to be proportional to $\text{Im}[\chi_{\text{TM}}(f)]/f$ (where χ_{TM} is the magnetic susceptibility of the FM sublattice) along a vector \mathbf{e} defined by the experimental geometry [20] [see Eq. (B7) in Appendix B]. The χ_{TM} is calculated analytically using Eq. (1) and a linear approximation of two LLG equations taken at the system's equilibrium (see Appendix B). Even if this method produces

TABLE I. Material parameters used in the model. The parameters marked with * were fixed.

	g_i	α_i	A_i (pJ/m)	D_i (mJ/m ²)	J (J/m ³)	K_i (kJ/m ³)
TM	2.10	0.015	11	-0.03	410 ⁷	2.0
RE	2 *	0 *	0 *	0 *		0 *

an analytical expression for the BLS spectrum, that expression is extremely cumbersome and was not directly fitted to the experimental data. Instead, it was used to verify that the model reproduces all the features of the spectra. The second method, based on the Smit-Beljers formalism [21,22], yields directly the resonance peak frequency and width. It consists in imposing a small oscillating solution to the linearized LLGs, producing a matrix equation, $\mathbf{M}_{\text{SB}}(f) \cdot \mathbf{u} = \mathbf{0}$, where \mathbf{u} is the vector of oscillation amplitudes. The frequency (f_0) and the width (δ) of the SW resonant modes correspond to, respectively, the real and imaginary parts of the roots of the polynomial $\det \mathbf{M}_{\text{SB}}(f) = 0$ (more details on both methods in Appendix B).

The material parameters of the energy model that underpins both approaches, shown in Table I, were manually fitted by iteratively comparing the model to the experimental spectra for all measured temperature and field conditions [shown in Fig. 3(e)]. To limit the number of free parameters, all parameters are constant in temperature except for the sublattice magnetizations, $M_{\text{TM}}(T)$ and $M_{\text{RE}}(T)$, extracted from the mean field model [Fig. 1(a)]. This approximation is justified by the small considered thermal interval (290–385 K), which is far from the Curie temperature (≈ 506 K). The contributions of Gd to DMI (D_{RE}), exchange stiffness (A_{RE}), and anisotropy (K_{RE}) were neglected as they are expected to be much smaller than those of FeCo [2,23,24], given that the Gd $4f$ moments do not participate directly in these mechanisms. The Gd g factor was fixed as $g_{\text{RE}} = 2.0$ [25,26]. The effects of the damping parameters (α_{RE} , α_{TM}) on the calculated spectra and mode frequencies were found to be indistinguishable. As it is expected that $\alpha_{\text{RE}} \ll \alpha_{\text{TM}}$ [27,28], α_{RE} was fixed at zero. The anisotropy (K_{TM}) was chosen to approximate the measured H_K at low fields and the reorientation points in the BLS measurements at higher fields [16]. The obtained g_{TM} is in the range of measurements of alloys with similar Fe:Co ratio [29]. The damping parameter α_{TM} is consistent with the domain wall mobilities found in Ref. [5], although it is probably overestimated as the model does not account for other sources of peak broadening (e.g., instrumental resolution and film inhomogeneities). The magnitudes of the remaining parameters (D_{TM} , J , A_{TM}) are consistent with measurements of similar materials [2,14,15].

The intensity calculated from $\chi_{\text{TM}}(f)$ [bottom panels of Fig. 1(c)] reproduces very well the experimental spectra, peak positions, widths, and relative amplitudes for the full range of temperatures, including in the reorientation range; it also shows a small asymmetry of comparable magnitude to the experimental values. In particular, it reproduces the change of relative amplitude of the S and AS peaks across T_{MC} observed experimentally (and discussed in Ref. [10]), as well as the large variation of peak width. The asymmetric Lorentzian

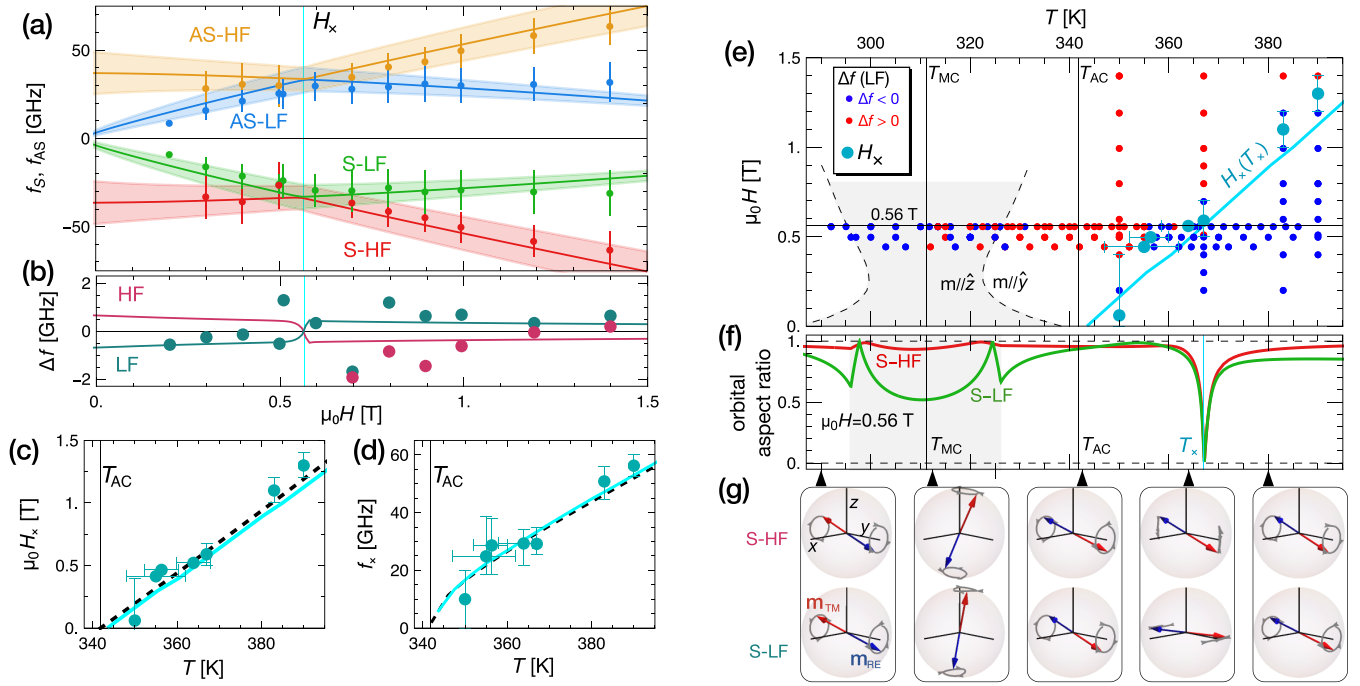


FIG. 3. (a) Mode frequencies (points) and widths (vertical bars) and (b) $\Delta f = |f_{AS}| - |f_S|$ vs H at $T = 367$ K, in the same color code as Fig. 2(a). (c) Mode-crossing field H_x and (d) frequency f_x vs T , measured experimentally (dots) and calculated (the full model in cyan, and the simplified model in black dashes). (e) Field and temperature of all the measured spectra, in blue dots when the LF's $\Delta f < 0$ and in red dots when it is > 0 . The mode crossing condition is shown by cyan dots (experimental) and line (Smit-Belgers method; for the S and AS modes). The gray zone is the calculated reorientation region. Its shape results from the anisotropy (at low field) and the spin-flop transition (at higher field; see Ref. [16]). (f) Orbital aspect ratio (from the model). (g) Trajectories and handedness calculated from the Smit-Belgers method, for the S mode at $\mu_0 H = 0.56$ T and different T (AS mode trajectories are similar). Amplitudes are increased for readability.

peaks also fit remarkably well the calculated spectra, which validates the choice of this fitting function.

The solid lines and shaded envelopes in Figs. 2(a) and 2(b) correspond to the mode frequencies and widths (respectively) calculated with the Smit-Belgers method. They reproduce very well the experimental frequencies and widths, including in the reorientation range, and at the crossing point where the frequency gap between HF and LF modes disappears [Fig. 2(a)]. The reversal of the Δf sign at T_{MC} and T_x is also obtained for both the LF and HF peaks [solid lines in Fig. 2(d)]. The deviation of the experimental Δf for the HF peaks is likely due to the low precision of Δf of these wide, low-amplitude peaks.

We observe that the mode-crossing temperature T_x varies with H [see Ref. [16] for measurements analogous to Fig. 2(a) at different values of H]. This variation is clearly revealed in Figs. 3(a) and 3(b), which show the peak frequencies and Δf versus H for a fixed temperature $T = 367$ K. The LF and HF modes cross and the sign of Δf is reversed at a field we name H_x , and here $\mu_0 H_x \approx 0.6$ T. The dependence of T_x on H demonstrates that it is not T_{AC} and thus that the mode crossing does not correspond to the compensation of angular momentum. We repeated these measurements for different temperatures. The variation of H_x versus T [cyan dots in Fig. 3(c)] suggests that $H_x \rightarrow 0$ as $T \rightarrow T_{AC}$. The frequency at the crossing point [f_x , Fig. 3(d)] also decreases as $T \rightarrow T_{AC}$. These features are reproduced by the model (cyan lines in the figures).

The elliptical orbits of the SW modes can also be deduced from the Smit-Belgers method by inspecting the null space of

$M_{SB}(f)$ (details in Appendix B). Figure 3(f) shows the aspect ratio of the elliptical orbits vs temperature, and some of the orbits are drawn in Fig. 3(g) (the gray arrows indicate their handedness). This permits us to interpret the changes of Δf around T_{MC} and T_x . Around T_{MC} , the continuous reorientation of the moments occurs without chirality change, which leads to the smooth reversal of the Δf sign seen experimentally [Fig. 2(d)]. At T_x , the elliptical orbits collapse into a linear oscillation with the LF mode orthogonal to the HF mode. Across this point, the SW chirality is reversed without reorientation, causing an abrupt reversal of the Δf sign [Figs. 2(d) and 3(b)].

B. Simplified model of ferrimagnetic resonance

To better understand the variation of the modes with the parameters, we consider a simplified energy model. Far from the reorientation range, the system's energy is dominated by J and H , and so we neglect all other energy terms as well as the damping. For $T > T_{MC}$ and below the spin-flop field (i.e., $\theta_{TM} \approx \frac{\pi}{2}$, $\theta_{RE} \approx \frac{3\pi}{2}$), the Smit-Belgers resonance frequencies of the AS modes are found to be

$$f_{HF/LF} = \sqrt{f_m^2 + \frac{1}{4}D^2} \pm \frac{1}{2}D,$$

$$2\pi D = J \left(\frac{\gamma_{TM}}{M_{TM}} - \frac{\gamma_{RE}}{M_{RE}} \right) + \mu_0 H (\gamma_{TM} + \gamma_{RE}), \quad (2)$$

$$2\pi f_m = \sqrt{\gamma_{TM}\gamma_{RE}} \sqrt{\mu_0 H \sqrt{J(M_{RE}^{-1} - M_{TM}^{-1})} - \mu_0 H}$$

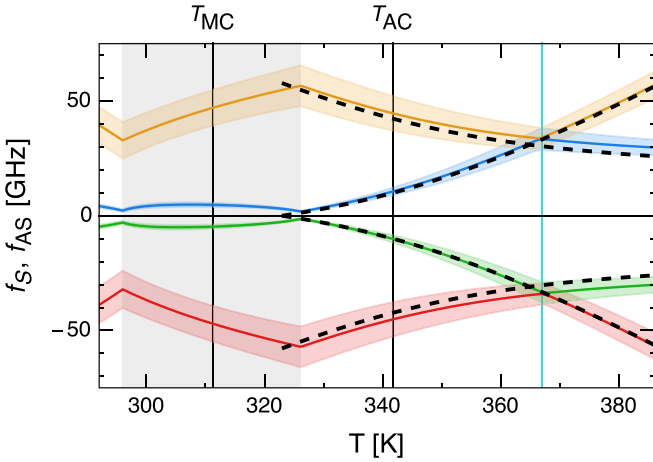


FIG. 4. Mode frequencies calculated with the full (solid lines and shading) and simplified (black dashed lines) energy models (with only J and H), for the same conditions and color code as in Fig. 3(a).

where $\gamma_i = g_i \mu_B / \hbar$ are the gyromagnetic ratios of the two sublattices, μ_B is the Bohr magneton, and \hbar is Planck's reduced constant (analogous expressions can be derived for the case $T < T_{MC}$). The frequencies of the S modes simply have the opposite sign of the AS modes under these approximations. These expressions show a good agreement with the experimental values and with the complete model (see Fig. 4 for a comparison). The simplified model fails where expected: in the reorientation range (where the anisotropy plays a major role), in the difference between the S and AS modes (caused by DMI), and in the variation of H_x with anisotropy (a very small effect in this system).

The crossing field H_x , for which $f_{HF} = f_{LF}$ ($D = 0$), can be analytically obtained, and reads

$$\mu_0 H_x = \frac{J}{\gamma_{TM} + \gamma_{RE}} \left(\frac{\gamma_{RE}}{M_{RE}} - \frac{\gamma_{TM}}{M_{TM}} \right). \quad (3)$$

This expression is plotted in black dashed lines in Figs. 3(c) and 3(d). The simplified model predicts that the mode crossing occurs above T_{AC} for a finite field or at T_{AC} (where $\frac{\gamma_{TM}}{M_{TM}} = \frac{\gamma_{RE}}{M_{RE}}$) if no field is applied.

The above results illustrate how ferrimagnetic SWs are fundamentally different from ferromagnetic or AF SWs. Although AFs also show two SW modes for a given k that may cross, the mode crossing can only occur at zero field, as the two AF sublattices are of the same nature. At that crossing point, the mode frequency is governed by the anisotropy and the interlattice exchange, fixed for a given material. In RE-TMs, the mode crossing occurs at a temperature-dependent field, and at a frequency that can be tuned with temperature.

Moreover, the intrinsic two-lattice nature of ferrimagnets makes it so that one-mode approximations cannot be valid over all the parameter range. This is true of the effective ferromagnet model, which diverges at T_{AC} , as well as of the exchange coupling mode approximation, which is zero at T_{AC} . A high-symmetry case, for which these models can be analytically solved, is described in Appendix A.

IV. CONCLUSION AND OUTLOOK

In summary, the ferrimagnetic SW dynamics show two modes with a complex variation with field and temperature, which opens the possibility for their use in faster and tunable spintronic devices. The presented model reproduces with excellent quantitative agreement the BLS spectra (namely, the complete amplitude versus frequency), as well as their thermal and field variation, which validates the underlying energy and dynamical model. The full fitting of BLS spectra shown here provides a powerful method to determine the energy and dynamics of ferrimagnetic alloys, adding a needed tool to study these materials that are harder to investigate than ferromagnets.

It would be interesting to apply this analysis to ferrimagnets containing REs other than Gd, with smaller Landé g factor or larger dissipation, for which fundamental questions remain open, including whether these REs affect precession [30]. Fundamentally different models have been proposed (by Wangsness [12], Kittel [30], and Van Vleck [31]) but could not be distinguished by analyzing the FMR spectra, which were limited to the LF peak. A quantitative analysis of the complete SW spectrum measured by BLS would provide a much stricter test of these models and would elucidate the dynamical behavior of these ferrimagnets.

Finally, the methodology described here is not limited to RE-TM ferrimagnets, and may be used to study other multilattice systems, containing or not REs, and even to noncollinear systems, such as weak ferromagnets, which are the focus of a recent interest for their use in spintronics [32].

ACKNOWLEDGMENTS

We acknowledge fruitful discussions with Stanislas Rohart, Laura Thevenard, and Catherine Gourdon. This work was supported by public grants overseen by the French National Research Agency (ANR) as part of the Investissements d'Avenir program Grants No. ANR-10-LABX-0035 (Labex NanoSaclay, projects FEMINIST and SPICY) and No. ANR-17-CE09-0030 (PIAF). The BLS experimental setup was funded by the Université Paris-Saclay (former research departments PhOM and EOE), the Institut de Physique (INP) of Centre National de la Recherche Scientifique (CNRS), ANR (Labex NanoSaclay, projects BLS@PSAY and SPICY), and the Île-de-France region (SESAME, Project No. EX039175 IMAGESPIN).

APPENDIX A: HIGH-SYMMETRY CASE

It is instructive to consider a simple high-symmetry case where the magnetization and anisotropy axis are aligned, for which simple analytical solutions can be derived. If all other energies are neglected, the mode frequencies given by the double-lattice model using the Smit-Beljers method are

$$f_{\pm} = \frac{1}{2}(f_{RE} - f_{TM}) \pm \frac{1}{2}\sqrt{(f_{TM} + f_{RE})^2 - 4J^2/(L_{TM}L_{RE})} \quad (A1)$$

where $2\pi f_{TM} = \frac{J+2K_{TM}}{L_{TM}}$ (likewise for f_{RE}) and $L_i = M_i/\gamma_i$. The mode crossing occurs when $f_{TM} = f_{RE}$ (as the square root is strictly positive), not necessarily at T_{AC} . This solution

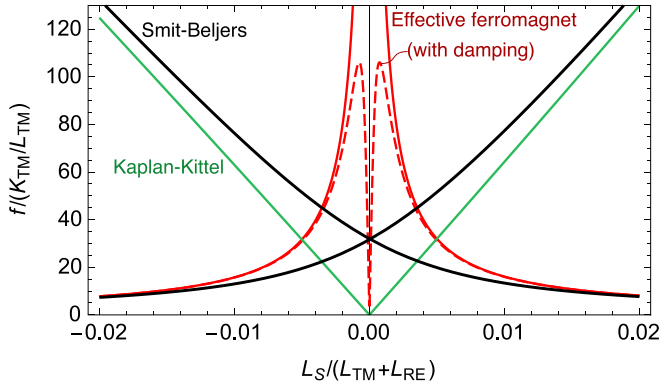


FIG. 5. Normalized absolute mode frequencies vs normalized angular momentum near angular compensation in a high-symmetry configuration calculated by different models: effective ferromagnet model with and without damping [12], the exchange coupling mode solution by Kaplan and Kittel [33], and the double-lattice Smit-Beljers model described before. The magnetization and anisotropy axis are parallel. The parameters (J, K_i, g_i) are those of Table I, except for $\alpha_{\text{TM}} = 0.0015$. All other energy terms are neglected.

is plotted near angular compensation in Fig. 5 (black lines), versus the normalized angular momentum [$L_S/(L_{\text{TM}} + L_{\text{RE}})$].

For this same case, the effective ferromagnet model [11,12] describes only one resonance with frequency given by

$$2\pi f_{\text{FM}} = \frac{L_S}{L_S^2 + L_\alpha^2} 2(K_{\text{TM}} + K_{\text{RE}}) \quad (\text{A2})$$

where $L_\alpha = \alpha_{\text{TM}}L_{\text{TM}} + \alpha_{\text{RE}}L_{\text{RE}}$ is the energy dissipation rate parameter [27,34]. At T_{AC} , this formula diverges as $1/L_S$ if the damping is neglected ($L_\alpha = 0$), or produces a double-polarity peak (with a node at T_{AC}) for a finite damping. In both cases, the frequency variation may be experimentally perceived as a peak of a single polarity if the sense of the magnetization precession is not accessible. Although the second resonance mode cannot be described by this model, its frequency can be estimated instead with Kaplan and Kittel's formula for the nondamped case [33]:

$$2\pi f_J = J \frac{L_S}{L_{\text{TM}}L_{\text{RE}}}. \quad (\text{A3})$$

Both solutions are shown in Fig. 5 (red and green curves, respectively).

It can be seen that the Smit-Beljers solutions approach the effective model far from compensation. The solutions are more similar the stronger the exchange coupling J and the more uncompensated the system is. However, near compensation, the solutions are very different. Unlike the effective

ferromagnet, the Smit-Beljers solution predicts a mode crossing at a finite frequency, which is at angular compensation only if the sublattices have equal energy terms. Therefore, in systems near angular compensation, with asymmetric sublattices, or with weak exchange coupling, the full solution of the coupled LLG equations should be used.

APPENDIX B: CALCULATION OF BLS SPECTRA

1. Linear approximation of the LLG equation with spin wave solutions

To calculate $\chi(f)$ as well as the Smit-Beljers solutions of the resonant spin wave modes, we consider a linear approximation of the LLG equation around the system's equilibrium uniform state. The magnetic state of a ferrimagnet with n sublattices is described by n unit vector fields \mathbf{m}_i ($n = 2$ in our case and $i = \text{TM}, \text{RE}$). Each sublattice i follows the LLG equation:

$$\dot{\mathbf{m}}_i = -\mu_0\gamma_i\mathbf{m}_i \times \mathcal{H}_i + \alpha_i\mathbf{m}_i \times \dot{\mathbf{m}}_i \quad (\text{B1})$$

where $\mathcal{H}_i = -\frac{\delta U/\delta \mathbf{m}_i}{\mu_0 M_i}$ is the effective field (specific to the sublattice i), and U is the total energy density of the system [Eq. (1)].

In the limit of small oscillations, \mathbf{m}_i can be decomposed in an equilibrium component \mathbf{m}_{0i} , spatially uniform and static, and a perpendicular component, spatially and time varying. Due to the geometry of our experiment [Fig. 1(b)], \mathbf{m}_{0i} lies in the (y, z) plane ($\mathbf{m}_{0i} = \cos \theta_i \hat{\mathbf{z}} + \sin \theta_i \hat{\mathbf{y}}$); the calculated θ_i are shown in Fig. 2(c) for $\mu_0 H = 0.56$ T, and the dynamical component lies in the (x, θ_i) plane:

$$\begin{aligned} \mathbf{m}_i &= \sqrt{1 - m_{ix}^2 - m_{i\theta}^2} \mathbf{m}_{0i} + m_{ix}(x, t) \hat{\mathbf{x}} + m_{i\theta}(x, t) \hat{\theta}_i \\ &= \left(1 - \frac{m_{ix}^2}{2} - \frac{m_{i\theta}^2}{2}\right) \mathbf{m}_{0i} + m_{ix}(x, t) \hat{\mathbf{x}} \\ &\quad + m_{i\theta}(x, t) \hat{\theta}_i + O(3) \end{aligned} \quad (\text{B2})$$

where $\hat{\theta}_i = \cos \theta_i \hat{\mathbf{y}} - \sin \theta_i \hat{\mathbf{z}}$. The dynamic component is assumed to follow a wave solution:

$$\begin{aligned} m_{ix}(x, t) &= \text{Re}(m_{ix} e^{i(kx - \omega t)}), \\ m_{i\theta}(x, t) &= \text{Re}(m_{i\theta} e^{i(kx - \omega t)}) \end{aligned}$$

where m_{ix} and $m_{i\theta}$ are complex and may show a phase difference. To determine m_{ix} and $m_{i\theta}$, the LLG equation is linearized around the equilibrium position \mathbf{m}_{0i} . Assuming the wave solution defined above and approximating in second order of $(m_{ix}, m_{i\theta})$, an effective field \mathcal{H}_i for the sublattice i is obtained (j represents the other sublattice):

$$\begin{aligned} \mu_0\gamma_i\mathcal{H}_i &= -\omega_{iA} \begin{pmatrix} m_{ix} \\ m_{i\theta} \cos \theta_i \\ -m_{i\theta} \sin \theta_i \end{pmatrix} + i\omega_{iD} \begin{pmatrix} m_{i\theta} \sin \theta_i \\ 0 \\ -m_{ix} \end{pmatrix} - \omega_{iJ} \begin{pmatrix} m_{jx} \\ m_{j\theta} \cos \theta_j + \sin \theta_j \\ -m_{j\theta} \sin \theta_j + \cos \theta_j \end{pmatrix} + \omega_{iK} (\cos \theta_i - m_{i\theta} \sin \theta_i) \hat{\mathbf{z}} \\ &\quad + \mu_0\gamma_i H \hat{\mathbf{y}} - [M_i \cos \theta_i + M_j \cos \theta_j - M_i m_{i\theta} \sin \theta_i - M_j m_{j\theta} \sin \theta_j] \hat{\mathbf{z}} - P_k \begin{pmatrix} M_i m_{ix} + M_j m_{jx} \\ 0 \\ M_i m_{i\theta} \sin \theta_i + M_j m_{j\theta} \sin \theta_j \end{pmatrix} + O(2) \end{aligned} \quad (\text{B3})$$

with $\omega_{iA} = \frac{\gamma_i 2A_i k^2}{M_i}$, $\omega_{iD} = \frac{\gamma_i 2D_i k}{M_i}$, $\omega_{iJ} = \frac{\gamma_i J}{M_i}$, $\omega_{iK} = \frac{\gamma_i 2K_i}{M_i}$, $P_k = 1 - (1 - e^{-|kd|})/|kd|$ [22], and d is the film thickness.

The wave solution and the effective field are then inserted in the LLG equation [Eq. (B1)], which becomes a linear equation with variables m_{ix} and $m_{i\theta}$, and can be written as a matrix product:

$$[M_{\text{SB}}(\omega)] \begin{pmatrix} m_{i,x} \\ m_{i,\theta} \\ \dots \end{pmatrix} = 0 \quad (\text{B4})$$

where $[M_{\text{SB}}(\omega)]$ is the Smit-Beljers square complex matrix. Thus, the resonance frequencies of the magnetic system are simply the roots of the fourth-degree polynomial: $P(\omega) = \det([M_{\text{SB}}(\omega)]) = 0$. The real and imaginary parts of these roots give, respectively, the frequency $2\pi f_0$ and the width $2\pi\delta$ of the associated peaks. Finally, the null space of $[M_{\text{SB}}(\omega)]$ gives the orbits (i.e., amplitude and ellipticity) of the SW modes associated to each frequency.

To calculate $\chi(\omega)$, an oscillating perturbing field \mathbf{h}_i with an amplitude $h_i \propto e^{i(kx - \omega t)}$ is included and the linearized LLG equation can be written as

$$[M_{\text{SB}}(\omega)] \begin{pmatrix} m_{ix} \\ m_{i\theta} \\ \dots \end{pmatrix} = [R(\theta_{\text{TM}}, \theta_{\text{RE}})] \begin{pmatrix} \gamma_{0i} h_{iX} \\ \gamma_{0i} h_{iY} \\ \gamma_{0i} h_{iZ} \\ \dots \end{pmatrix} \quad (\text{B5})$$

where $[R(\theta_{\text{TM}}, \theta_{\text{RE}})]$ is a 4×6 projection matrix that only depends on the θ_i angles. By solving this linear system, it is then possible to calculate the susceptibility 6×6 tensor χ defined such as

$$\begin{pmatrix} \mathbf{m}_i \\ \dots \end{pmatrix} = \begin{pmatrix} \mathbf{m}_{0i} \\ \dots \end{pmatrix} + [\chi] \begin{pmatrix} \mathbf{h}_i \\ \dots \end{pmatrix}. \quad (\text{B6})$$

The tensor χ and the Smit-Beljers matrix are related by $M_{\text{SB}} = R^{-1} \cdot \chi^{-1} \cdot R$.

2. Calculation of the backscattered spectrum

The intensity I of the backscattered light by a spin wave at an angular frequency ω depends on the amplitude of the spin

TABLE II. Material optical constants (refraction index n and extinction coefficient κ) used to calculate ϵ .

	Si	SiOx	GdFeCo	Al	AlOx
n	4.1520	1.4607	2.46	0.93878	1.7717
κ	0.051787	0	2.89	6.4195	0

wave, on the strength of the magneto-optical effect, and on the amplitudes of the electric fields in the magnetic film associated with the incident light (\mathbf{E}_i) and with the backscattered light (\mathbf{E}_{BS}).

Due to the linear magneto-optical effect, \mathbf{E}_i excites an electric polarization $\mathbf{P} = iQ\mathbf{E}_i \times \mathbf{m}$, where $Q\mathbf{m}$ is the magneto-optical gyration vector (which is only significant for the TM sublattice [4]). As \mathbf{E}_i oscillates at angular frequency Ω and \mathbf{m} oscillates at ω , \mathbf{P} will oscillate at $\Omega \pm \omega$. The (complex) amplitude A of the backscattered light at $\Omega \pm \omega$ is given by the projection of \mathbf{E}_{BS} on the direction of \mathbf{P} , $A \propto \mathbf{E}_{\text{BS}}^* \cdot \mathbf{P} = iQ\mathbf{m} \cdot (\mathbf{E}_{\text{BS}}^* \times \mathbf{E}_i) = iQ\mathbf{m} \cdot \mathbf{e}$, with $\mathbf{e} \equiv \mathbf{E}_{\text{BS}}^* \times \mathbf{E}_i$. In the geometry of the experiment, the incident light is s polarized ($\mathbf{E}_i \parallel \hat{\mathbf{y}}$) and the analyzed backscattered light is p polarized ($\mathbf{E}_{\text{BS}} \perp \hat{\mathbf{y}}$), and so $\mathbf{e} = E_{i,y}(-E_{\text{BS},z}^*, 0, E_{\text{BS},x}^*)$. The intensity of the backscattered light $I = |A|^2 = |Q|^2 |\mathbf{m} \cdot \mathbf{e}|^2$ can be deduced using the fluctuation-dissipation theorem applied to $\mathbf{m} \cdot \mathbf{e}$ [20]:

$$I \propto \frac{1}{\omega} \text{Im}(\mathbf{e}^* \cdot \chi \cdot \mathbf{e}) = \frac{1}{\omega} (\chi''_{xx} |E_{z,\text{BS}}|^2 + \chi''_{zz} |E_{x,\text{BS}}|^2 + \text{Im}[\chi_{xz} E_{z,\text{BS}} E_{x,\text{BS}}^* + \chi_{zx} E_{x,\text{BS}} E_{z,\text{BS}}^*]) \quad (\text{B7})$$

where $\chi = \chi' + i\chi''$ is the material's susceptibility. The relative magnitude and phase of $E_{x,\text{BS}}$ and $E_{z,\text{BS}}$ were calculated taking into account the angle of incidence, and the electric permittivities and thicknesses of the layers that compose the film with the classical boundary conditions (see Table II).

- [1] B. Dieny, I. L. Prejbeanu, K. Garello, P. Gambardella, P. Freitas, R. Lehdorff, W. Raberg, U. Ebels, S. O. Demokritov, J. Akerman *et al.*, *Nat. Electron.* **3**, 446 (2020).
- [2] P. Hansen, C. Clausen, G. Much, M. Rosenkranz, and K. Witter, *J. Appl. Phys.* **66**, 756 (1989).
- [3] Y. Hirata, D.-H. Kim, T. Okuno, T. Nishimura, D.-Y. Kim, Y. Futakawa, H. Yoshikawa, A. Tsukamoto, K.-J. Kim, S.-B. Choe, and T. Ono, *Phys. Rev. B* **97**, 220403(R) (2018).
- [4] E. Haltz, R. Weil, J. Sampaio, A. Pointillon, O. Rousseau, K. March, N. Brun, Z. Li, E. Briand, C. Bachelet, Y. Dumont, and A. Mougin, *Phys. Rev. Mater.* **2**, 104410 (2018).
- [5] E. Haltz, J. Sampaio, S. Krishnia, L. Berges, R. Weil, and A. Mougin, *Sci. Rep.* **10**, 16292 (2020).
- [6] S. Geschwind and L. R. Walker, *J. Appl. Phys.* **30**, S163 (1959).
- [7] J. Paulevé, *J. Appl. Phys.* **29**, 259 (1958).
- [8] M. Binder, A. Weber, O. Mosendz, G. Woltersdorf, M. Izquierdo, I. Neudecker, J. R. Dahn, T. D. Hatchard, J. U. Thiele, C. H. Back, and M. R. Scheinfein, *Phys. Rev. B* **74**, 134404 (2006).
- [9] C. D. Stanciu, A. V. Kimel, F. Hansteen, A. Tsukamoto, A. Itoh, A. Kirilyuk, and T. Rasing, *Phys. Rev. B* **73**, 220402 (2006).
- [10] C. Kim, S. Lee, H.-G. Kim, J.-H. Park, K.-W. Moon, J. Y. Park, J. M. Yuk, K.-J. Lee, B.-G. Park, S. K. Kim, K.-J. Kim, and C. Hwang, *Nat. Mater.* **19**, 980 (2020).
- [11] N. Tsuya, *Prog. Theor. Phys.* **7**, 263 (1952).
- [12] R. K. Wangsness, *Phys. Rev.* **91**, 1085 (1953).
- [13] A. F. Andreev and V. I. Marchenko, *Sov. Phys. Usp.* **23**, 21 (1980).
- [14] S. Krishnia, E. Haltz, L. Berges, L. Aballe, M. Foerster, L. Bocher, R. Weil, A. Thiaville, J. Sampaio, and A. Mougin, *Phys. Rev. Appl.* **16**, 024040 (2021).
- [15] D. H. Kim, M. Haruta, H. W. Ko, G. Go, H. J. Park, T. Nishimura, D. Y. Kim, T. Okuno, Y. Hirata, Y. Futakawa *et al.*, *Nat. Mater.* **18**, 685 (2019).

- [16] See Supplemental Material at <http://link.aps.org/supplemental/10.1103/PhysRevB.105.104414> for more details on the reorientation of ferrimagnets, BLS method, and for additional data (spectra at different temperatures and fields).
- [17] K. Di, V. L. Zhang, H. S. Lim, S. C. Ng, M. H. Kuok, J. Yu, J. Yoon, X. Qiu, and H. Yang, *Phys. Rev. Lett.* **114**, 047201 (2015).
- [18] M. Belmeguenai, J.-P. Adam, Y. Roussigné, S. Eimer, T. Devolder, J.-V. Kim, S. M. Cherif, A. Stashkevich, and A. Thiaville, *Phys. Rev. B* **91**, 180405 (2015).
- [19] D. Cortés-Ortuño and P. Landeros, *J. Phys.: Condens. Matter* **25**, 156001 (2013).
- [20] Y. Roussigné, F. Ganot, C. Dugautier, P. Moch, and D. Renard, *Phys. Rev. B* **52**, 350 (1995).
- [21] J. Smit and H. G. Beljers, *Philips Res. Rep.* **10**, 113 (1955).
- [22] B. A. Kalinikos and A. N. Slavin, *J. Phys. C* **19**, 7013 (1986).
- [23] R. C. Taylor and A. Gangulee, *J. Appl. Phys.* **48**, 358 (1977).
- [24] A. Gangulee and R. J. Kobliska, *J. Appl. Phys.* **49**, 4896 (1978).
- [25] Y. Ogata, H. Chudo, M. Ono, K. Harii, M. Matsuo, S. Maekawa, and E. Saitoh, *Appl. Phys. Lett.* **110**, 072409 (2017).
- [26] J. S. Thorp and M. D. Hossain, *J. Mater. Sci.* **16**, 633 (1981).
- [27] G. P. Vella-Coleiro, in *Magnetism and Magnetic Materials — 1972: Eighteenth Annual Conference*, edited by H. C. Wolfe, C. D. Graham, and J. J. Rhyne, AIP Conf. Proc. No. 10 (AIP, New York, 1973), p. 424.
- [28] G. Woltersdorf, M. Kiessling, G. Meyer, J.-U. Thiele, and C. H. Back, *Phys. Rev. Lett.* **102**, 257602 (2009).
- [29] T. Devolder, P.-H. Ducrot, J.-P. Adam, I. Barisic, N. Vernier, J.-V. Kim, B. Ockert, and D. Ravelosona, *Appl. Phys. Lett.* **102**, 022407 (2013).
- [30] C. Kittel, *Phys. Rev.* **115**, 1587 (1959).
- [31] J. H. Van Vleck, *Phys. Rev.* **123**, 58 (1961).
- [32] I. Boventer, H. T. Simensen, A. Anane, M. Kläui, A. Brataas, and R. Lebrun, *Phys. Rev. Lett.* **126**, 187201 (2021).
- [33] J. Kaplan and C. Kittel, *J. Chem. Phys.* **21**, 760 (1953).
- [34] E. Haltz, S. Krishnia, L. Berges, R. Weil, A. Mougin, and J. Sampaio, *Phys. Rev. B* **103**, 014444 (2021).